EBioMedicine 50 (2019) 93–102

Contents lists available at ScienceDirect

EBioMedicine

journal homepage: www.elsevier.com/locate/ebiom

Research paper

Image-guided surgery of head and neck carcinoma in rabbit models by intra-operatively defining tumour-infiltrated margins and metastatic lymph nodes

Pengpeng Sun[a,1], Yunfei Zhang[b,c,1], Kaicheng Li[a,d,1], Cong Wang[b], Feng Zeng[b,e], Jinyu Zhu[a,f], Yingwei Wu[a,*], Xiaofeng Tao[a,*]

[a] Department of Radiology, School of Medicine, Shanghai Ninth People's Hospital, Shanghai Jiao Tong University, 639 Zhizao Ju Road, Shanghai 200011, China
[b] School of Pharmacy, Key Laboratory of Smart Drug Delivery, Ministry of Education, Fudan University, Shanghai 201203, China
[c] United Imaging Healthcare, Shanghai, 201807, China
[d] Department of Radiology, Hainan West Central Hospital, Dan Zhou, Hai Nan, 571700, China
[e] Pi-Wei Institute, Guangzhou University of Chinese Medicine, Guangzhou, 510405, China
[f] Department of Radiology, Shanghai Six People's Hospital, Shanghai Jiao Tong University, Shanghai 200233, China

ARTICLE INFO

Article history:
Received 13 September 2019
Revised 26 October 2019
Accepted 28 October 2019
Available online 13 November 2019

Keywords:
Surface-enhanced resonance Raman scattering (SERRS)
Magnetic resonance imaging (MRI)
Head and neck squamous cell carcinoma (HNSCC)
Lymph node metastasis
Image-guided resection

ABSTRACT

Background: The infiltrative nature and lymphatic metastasis of head and neck squamous cell carcinoma (HNSCC) are the main reasons leading to its poor prognosis.

Methods: A multimodal surface-enhanced resonance Raman spectroscopy (SERRS) and magnetic resonance (MR) nanoprobe, in which paramagnetic chelators and heptamethine cyanine-based Raman reporter molecules were functionalized on a gold nanostar (AuS) surface was developed. Preoperative MRI and intraoperative SERRS-guided surgery were performed on rabbits bearing head and neck VX2 tumours to determine feasibility of the MR/SERRS probe in defining tumour marginal infiltration and lymph nodes metastasis.

Findings: Preoperative T1-weighted MRI (T1W-MRI) unambiguously delineated the orthotopic head and neck VX2 tumour xenograft and detected the metastatic lymph nodes in rabbit models after intravenous administration of the probe. With the assistance of a hand-held Raman detector, the probe not only intra-operatively demarcated invasive tumour margins but also successfully distinguished metastatic lymph nodes via a remarkable attenuated Raman signal. Importantly, the group of rabbits subjected to the SERRS-guided surgery exhibited prolonged median survival time (78 days) compared with that of the control group without surgical intervention (29 days) or the group treated with conventional white-light-guided surgery (42 days) ($P < 0.0001$).

Interpretation: we developed a novel AuS-based multimodal MR/SERRS probe. The capability of this probe to identify both a tumour xenograft and metastatic lymph nodes preoperatively by MRI and intra-operatively by SERRS not only avoids the need for unnecessary resection of neurological structures but also provides a new opportunity to improve the surgical prognosis of head and neck carcinoma of infiltrative nature.

1. Introduction

Head and neck squamous cell carcinoma (HNSCC) is the sixth leading cancer worldwide, having an annual incidence of approximately 600,000 cases with 40–50% mortality [1]. HNSCC may be treated by surgical resection, radiation therapy, chemotherapy, or combinations of these approaches. Despite advances in therapeutic management, the survival time for HNSCC has not been greatly improved over the past several decades [2,3]. Local recurrence and cervical lymph node metastasis are major reasons for the poor prognosis of HNSCC. The limited narrow space and extensive neurovascular plexus in the head and neck area make it highly complicated to acquire clear pathological margins, and thus, functional

* Corresponding authors.
E-mail addresses: wuyw0103@hotmail.com (Y. Wu), cjr.taoxiaofeng@vip.163.com (X. Tao).
[1] These authors share equal first authorship.

https://doi.org/10.1016/j.ebiom.2019.10.055

Research in context

Evidence before this study

Although debulking surgery is a mainstay treatment for HNSCC, locoregional recurrence and early metastasis are inevitable due to the difficulty in intra-operatively excising the tumour infiltrative margins without damaging adjacent neurological structures. SERRS has ultra-high sensitivity, reaching picomolar or even femtomolar levels and thus endowing it with great potential, especially in SERRS-guided tumour resection. Fascinatingly, due to the superior ability of SERRS to define infiltrative margins in real time and the ability of MRI to preoperatively locate tumours and preliminarily evaluate malignancy with high soft-tissue resolution, the combination of SERRS and MRI holds unprecedented potential for guiding tumour resection of HNSCCs far more accurately and completely.

Added value of this study

The MR/SERRS nanoprobe with multi-modal potential developed in this study enabled preoperative MRI and intra-operative image-guided resection of head and neck tumour xenografts by virtue of the SERRS effect. The ability of the nanoprobe to precisely define infiltrative tumour margins and metastatic lymph nodes would markedly reduce the need for unnecessary resection in the head and neck area and profoundly improve the surgical prognosis of head and neck carcinoma.

Implications of all the available evidence

Current available evidence implicates that combination of MRI and SERRS would allow surgeons, before and during surgery, to point tumor infiltrative boundaries of primary carcinomas more precisely and therefore improve surgical prognosis. This represents a promising avenue for applying multimodal imaging strategy in patients involved with malignant tumors.

disorders resulting from extensive resections are inevitable. Even worse, the infiltrative tumour margins of HNSCC add complexity for surgeons to completely remove neoplastic tissues intra-operatively. For example, satellite foci in adjacent normal tissues are not visualized during surgical operation [4]. In addition, identification of cervical lymph node metastasis is highly crucial for surgeons since neck dissection is required for HNSCC patients with the initial presentation of cervical lymph node metastasis and will profoundly influence their prognosis. Although several imaging criteria have been proposed, distinguishing metastatic lymph nodes from inflammatory or reactive lymph nodes either by magnetic resonance imaging (MRI) or by CT is still challenging due to the current size-dependent criteria [5]. Therefore, the surgical prognosis of HNSCC would greatly benefit from a more accurate intra-operative approach to access resection margins. The increased precision of imaging the true extent of tumour spread could markedly reduce the need for unnecessary resection of surrounding normal tissue.

Imaging modalities and techniques that allow surgeons to perform preoperative imaging of HNSCC prior to surgery are now being developed. Among these, MRI is the most favourable imaging modality for evaluating primary neoplasms in the head and neck because of its high spatial resolution for soft tissue. The large footprint and long acquisition time of the MRI modality, however, largely limit its applications as an intra-operative imaging-guided approach [6,7]. Compared to the MRI modality, optical imaging methods have the advantages of high sensitivity, relatively low cost and abundant availability. Sophisticated imaging-guided surgical resection may allow surgeons to more precisely pinpoint tumour margins both prior to and during surgery and therefore improve surgical resection completeness, especially for tumours with infiltrative margins and invasive growth patterns such as HNSCC.

Through the incorporation of roughened metallic surfaces as enhancing substrates, the surface-enhanced Raman scattering (SERS) technique can yield up to 10^6~10^{10} times enhancement in signal compared to that of the traditional Raman technique [8]. Moreover, compared to fluorescence imaging, SERS has other intrinsic advantages, including its multiplexing capability originating from fingerprint-like spectra, high sensitivity, and enhanced photostability, which render SERS a powerful tool, especially for bio-applications such as the detection of molecular biomarkers and tumour diagnosis. By applying special molecular reporters with absorption energy similar to the incident laser, surface-enhanced resonance Raman spectroscopy (SERRS) yields an extra 10^2~10^3 times signal enhancement relative to that provided by SERS [8]. Therefore, SERRS not only inherits the aforementioned advantages but also has far higher sensitivity than conventional SERS, reaching picomolar or even femtomolar levels and thus endowing it with great potential, especially in SERRS-guided tumour resection [9,10]. Fascinatingly, due to the superior ability of SERRS to define infiltrative margins in real time because of its ultrahigh sensitivity and the ability of MRI to preoperatively locate tumours and preliminarily evaluate malignancy with high soft-tissue resolution, previous works reported that the combination of SERRS and MRI holds unprecedented potential for guiding the resection of gliomas far more accurately and completely [7,8].

To the best of our knowledge, no research on guiding the resection of HNSCCs via the combination of SERRS and MRI has been published. As mentioned above, the characteristics of infiltrative growth and lymph node metastasis make resection of HNSCCs a notoriously troublesome task for clinical surgeons. Therefore, for the first time, this study aims to develop a multifunctional MRI-SERRS nanoprobe that integrates the advantages of SERRS and MRI to improve surgical management of HNSCCs (Fig. 1).

2. Materials and methods

2.1. Synthesis and characterization

AuS: Gold nanostars (AuSs) were prepared according to protocols in our previous work [9]. Briefly, gold seeds with an average diameter of 12 nm were obtained by adding 15 mL of citrate solution (1%) to 100 mL of boiling chloroauric acid aqueous solution (1.0 mM). Next, 1 mL of HCl (0.1 M) and 4.0 mL of gold seed solution were added to 200 mL of chloroauric acid (0.25 mM). Then, 2.0 mL of $AgNO_3$ (3.0 mM) and 1.0 mL of ascorbic acid (100 mM) were simultaneously added to the previous mixture under continuous vigorous stirring for 30 s to harvest the AuSs. AuS-Gd: Diethylenetriaminepentaacetic (DTPA) dianhydride (10 mg, 28 μM) and 2-aminoethanethiol (2.1 mg, 28 μM) were mixed in 1.0 mL of anhydrous dimethylformamide (DMF) and stirred at room temperature for 4 h to yield DTPA-SH, which was then added to the AuS solution with $GdCl_3{\cdot}6H_2O$ successively and stirred lightly overnight. AuS-Cy7-Gd: Cy7-SH is a type of heptamethine cyanine dye-based Raman reporter previously developed in our work [11]. Cy7-SH and $mPEG_{2000}$-SH were successively added to the AuS solution (Cy7-SH/$mPEG_{2000}$-SH/AuS: 1500/10,000/1) and stirred lightly overnight, and the resulting product was purified by dialysis (10,000 MW cut-off dialysis bag) to obtain the AuS-Cy7-Gd nanoprobe. The nanoprobe was characterized by UV−vis spectroscopy

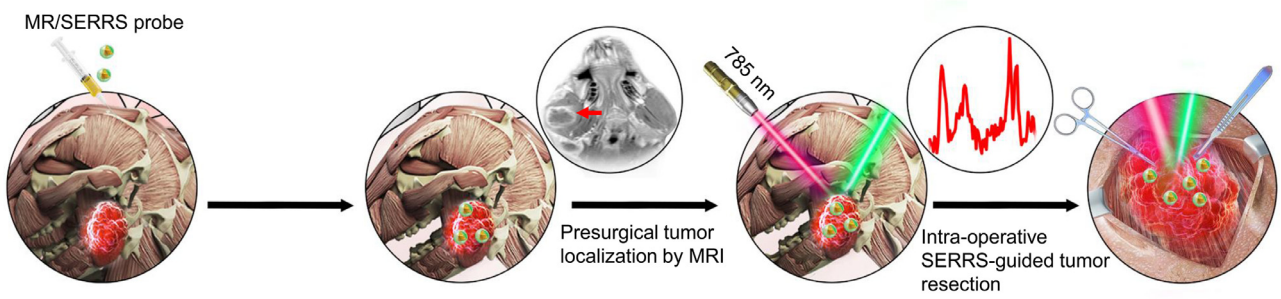

Fig. 1. Schematic illustration of image-guided surgery of head and neck orthotopic tumour xenografts in rabbit models. A multimodal MR/SERRS nanoprobe that not only preoperatively defined the tumour position by MRI but also intra-operatively guided tumour resection via an ultra-sensitive SERRS signal was developed.

(UV-2550; Shimadzu, Japan), dynamic light scattering (Zetasizer 3000; Malvern Instruments), and transmission electron microscopy (TEM) (Tecnai G2spirit Biotwin, FEI). X-ray photoelectron spectroscopy (XPS) (ESCALAB 250XI, Thermo) was performed for both AuNP and AuNP-Gd to ensure that Gd chelators were successfully conjugated to AuNP. The Gd^{3+} concentration in the nanoprobe was determined by a Hitachi P-4010 inductively coupled plasma atomic emission spectroscopy system (Tokyo, Japan). The longitudinal relaxivity R_1 values of the nanoprobe were calculated by plotting 1/T1 versus the concentration of Gd^{3+} in the nanoprobe with one 1.5 T MR scanner (uMR560, United Imaging Healthcare, Shanghai, China).

2.2. Correlation between Raman signal intensity and tissue depth

To obtain the signal intensity correlation to the tissue depth, the masseter muscle phantoms were created. The masseter muscle from a sacrificed 8-week-old rabbit ($n = 3$) was removed, cleaned and fixed in 4% PFA for 24 h. With the help of micrometer caliper, the fixed muscle tissues were cut into slices with thickness of 0.3, 0.5, 0.7, 1.0, 1.3, 1.5 and1.7 mm, respectively. 200 ul AuS-Cy7-Gd solution (200 pM) in a small round dish and was covered with muscle slices of different thickness. Actual Raman intensity values were recorded and used to produce the scaled graph.

2.3. Cell cultures

VX-2 carcinoma cells (originated from rabbits), PC-12 cells (originated from a pheochromocytoma of the rat adrenal medulla) and oral mucosal epithelial cells of rabbits were kindly provided by the Department of Radiology of Shanghai First People's Hospital. All cells used in this study were cultured in DMEM containing 10% foetal bovine serum (FBS), streptomycin and 1% penicillin (37 °C, 5% CO_2).

2.4. Cell viability

Cell viability was evaluated by means of the CCK-8 assay with VX2 cells, PC-12 cells and oral mucosal epithelial cells. After incubation with AuNS-Cy7-Gd at various concentration (range 0–150pM/ml) for 48 h, cell viability was calculated by determining the OD via an enzyme-labelled instrument (Tecan-200 Infinite Proreader, Nuremberg, Bavaria, Germany)

2.5. Ex vivo cell phantoms

MR images of the AuNS-Cy7-Gd treated VX-2 tumor cells were obtained. VX-2 tumor cells with 100% confluence received fresh medium right before AuS-Cy7-Gd treatment. AuS-Cy7-Gd (2 mmol/L) was added into 10-cm dish for 24 h with 5% CO_2 at 37 °C. The cells were then washed with PBS for three times to remove free nanoprobe. The cells were counted and sent to inductively coupled plasma mass spectrometry (ICP-MS, Cantest, Burnaby, BC) for determination of total Gd content. Various number of cells (range: 0–4500 K cells) were prepared in 0.5 ml agarose gel for ex vivo cell phantoms. Spine echo (SE) sequence was applied on the 1.5 T canner (uMR560, United Imaging Healthcare, Shanghai, China) and correlations between 1/T1 and cell numbers were evaluated.

2.6. Side effects of the nanoprobe

The nanoprobe was intravenously administered via the ear vein of the rabbits. The major organs, including heart, liver, spleen, lung and kidney tissues, were harvested, sectioned with a thickness of 5 μm and then stained with haematoxylin and eosin (H&E) for pathological analysis.

2.7. Establishment of the VX2 tumour model

Animal experiments were performed in compliance with the policy on animal use and ethics established by the Ethics Committee of Shanghai Ninth People's Hospital. VX2 tumour models were established according to procedures in our previous study with slight modifications [12]. Briefly, VX2 tumours were initially grown in the right hind limb of a donor rabbit (maintained at our institute). The donor rabbit, bearing a VX2 tumour that was approximately 2 cm in diameter, was anaesthetized with pentobarbital sodium (30 mg/kg). After shaving and disinfection, the tissue from the tumour margin was resected and washed twice with normal saline (NS) to remove blood and necrotic tissue. Then, the tumour tissue was cut into small pieces with scissors and added to NS. After filtering with a 200-mesh stainless steel screen, VX2 tumour suspensions were prepared for the following study. After anaesthesia induction, the right maxillofacial region of each rabbit in our study was shaved and disinfected. Then, 0.2 mL (2×10^8 cells) of the VX2 tumour suspension as prepared above was injected into the deep masseter muscle, approaching the angle of the mandible at approximately 1 cm [13]. The inoculated rabbits were fed regular food and water during the tumour growth period.

2.8. Preoperatively imaging HNSCC by MRI

When the tumours grew to approximately 3 cm in diameter four weeks post-inoculation, MR scanning was performed on a 3 Tesla clinical MRI scanner using a knee coil (MAGNETOM Verio, Siemens AG, Germany). The rabbits were placed in the prone position and scanned with both pre- and post-contrast coronal T1-weighted imaging (T1WI). The T1WI acquisition parameters were as follows: spine echo (SE) sequence, field of view (FOV) of 120 mm × 120 mm, matrix of 256 × 160, repetition time (TR)/echo

time (TE) of 350/15 ms, slice thickness of 1.0 mm, slice interval of 0.5 mm, and number of excitations (NEX) of 2. Contrast-enhanced imaging was performed with the same parameters as T1WI. The contrast-enhanced T1WI image was obtained 20 min post-intravenous administration of AuS-Cy7-Gd via the ear vein (0.05 mmol [Gd^{3+}] per kg) followed by injection of 2 mL of NS.

Determination of the normalized signal intensity (SI) before and after enhanced scanning of tumours: regions of interest were determined by plain scanning and contrast-enhanced T1WI, and the SI was measured in the solid region of the tumour and contralateral normal masseter muscle tissue. The corresponding normalized SI was calculated and expressed as the mean ± standard deviation. The normalized SI values before and after enhancement were expressed as SI_{pre} ($SI_{tumour\ pre}/SI_{muscle\ pre}$) and SI_{post} ($SI_{tumour\ post}/SI_{muscle\ post}$), respectively.

Determination of the normalized SI before ($SI_{lymph\ node\ pre}/SI_{muscle\ pre}$) and after ($SI_{lymph\ node\ post}/SI_{muscle\ post}$) enhanced scanning of lymph nodes: the region of interest was determined according to the whole lymph node and normal masseter muscle tissue by plain scanning and enhanced T1WI. Meanwhile, the SI was measured. The corresponding normalized SI values were calculated and expressed as the mean ± standard deviation. The difference between plain scanning and enhanced scanning of metastatic lymph nodes was statistically analysed.

2.9. Intra-operatively guiding HNSCC resection with the aid of SERRS

All of the rabbits bearing VX2 tumours were randomly divided into two groups ($n = 10$) as follows: (1) the SERRS-guided tumour surgery group, referring to the group subjected to intra-operative Raman-guided surgical resection of the primary tumour and removal of cervical metastatic lymph nodes, and (2) the white-light illumination surgery group, referring to the group for which tumour resection was performed under white-light illumination but without SERRS guidance and suspected cervical metastatic lymph nodes were removed according to the standard neck dissection protocol. For the SERRS-guided group, the rabbits bearing VX2 tumours were injected with AuS-Cy7-Gd via the ear vein. After 24 h, blood samples from the ear vein were obtained to detect the characteristic SERRS peak (509 cm^{-1} and 541 cm^{-1}) in order to ensure that there was no distinctive characteristic SERRS signal in the blood flow. Afterwards, step-by-step SERRS-guided real-time surgery was performed using a hand-held Raman scanner (Ocean Optics Inc. QE65 Pro, USA) with a 785-nm excitation laser, a laser power of 400 mW, and a penetration depth of 5.0 mm. The acquisition time for each measurement was 100 ms. First, a 90-degree Raman laser beam was oriented towards the tumour, and tissues with distinctive SERRS signals (characteristic double peaks at 509 cm^{-1} and 541 cm^{-1}) were removed in succession. Next, the tumour resection bed, tumour marginal areas and surrounding tissues were explored using the laser probe via variable imaging orientation until the SERRS signals were less than a threshold. The SERRS SI of normal muscles was used as the signal threshold. Furthermore, SERRS spectra of each lymph node were recorded using a hand-held Raman scanner. Scanning was performed by holding the hand-held probe in variable imaging orientation with an approximate distance to the lymph nodes of 5 mm. To more accurately identify partial metastatic lymph nodes, scanning was performed three times to ensure that the whole lymph node was covered. Resected tissue and lymph nodes from both surgical approaches were sectioned for further histological analysis.

2.10. Histological analysis

Histological analysis was performed to validate the accuracy of the SERRS-guided surgical approach. After the surgical resection was finished, tissues in the tumour resection bed and lymph nodes were fixed in 4% paraformaldehyde overnight for paraffin embedding at 4 °C. Tissues were sectioned into 5-μm-thick slices and subsequently processed for H&E staining. Additionally, immunohistochemistry was performed to detect Ki67 immunoreactivity to determine cellular proliferation. Slides were visualized under an optical microscope.

2.11. In vivo accumulation of AuS-Cy7-Gd via TEM

The distribution of AuS-Cy7-Gd was investigated via TEM. Fresh tumour tissue was fixed with 2.5% glutaraldehyde solution overnight and 1% osmium peroxide for 1 h. Then, an ethanol solution (50, 70, 80, 90, 95, 100, and 100%) was used to dehydrate the specimen 7 times for 15 min each time. The tissue was embedded in ethoxyline resin 812 and sectioned by a microtome at a thickness of 200 nm. A Tecnai G2 Spirit BioTWIN microscope was used to obtain TEM images from 120-kV scans after uranium acetate staining for 10 min and 5% lead citrate staining for 5 min.

2.12. Raman microscopic imaging

To further validate the tumour margins and infiltration, an in vitro confocal Raman imaging study was performed. Tissues were processed and sectioned with the same procedures as those used for histological analysis. Confocal Raman imaging was conducted using an XploRA confocal Raman spectrometer (HORIBA, Japan) with a 50X objective lens. The 785-nm excitation laser was kept at a power output of approximately 80 mW, and Raman spectroscopic mapping images were obtained by quantifying the intensity of the characteristic Raman peak of nanoparticles at 510 cm^{-1}, with steps of 10 μm and an acquisition time of 1.0 s. Tumour margins delineated via confocal Raman imaging were compared with H&E staining images.

2.13. Survival and prognosis evaluation

To determine how surgical resection approaches affected tumour survival and prognosis, 35 rabbits were randomly divided into three groups: the control group (no therapy), $n = 10$; the white-light illumination resection group, $n = 10$; and the SERRS-guided resection group, $n = 15$. The observation period was 90 days. Rabbits that underwent tumour surgery were returned to their cages for feeding and received antibiotics according to common use. For rabbits that underwent surgical resection, survival was closely monitored until their deaths occurred. Then, the tumour resection beds were removed to determine the residue rate via histological analysis. For the control group, all rabbits were sacrificed when the observation period ended.

2.14. Statistical analysis

All statistical analyses were performed using the GraphPad Prism 5 software package (La Jolla, CA, USA). P values less than 0.05 were considered statistically significant ($^{*}P < 0.05$, $^{**}P < 0.01$, $^{***}P < 0.001$).

3. Results

3.1. Synthesis, characterization and safety evaluation of the multi-modal MR/SERRS nanoprobe

The multifunctional MRI-SERRS nanoprobe developed in this work, termed AuS-Cy7-Gd, had an average diameter of 60 nm. The synthesis of the nanoprobe is described in Fig. 2. Briefly, DTPA-SH was obtained through acylation between DTPA dianhydride and

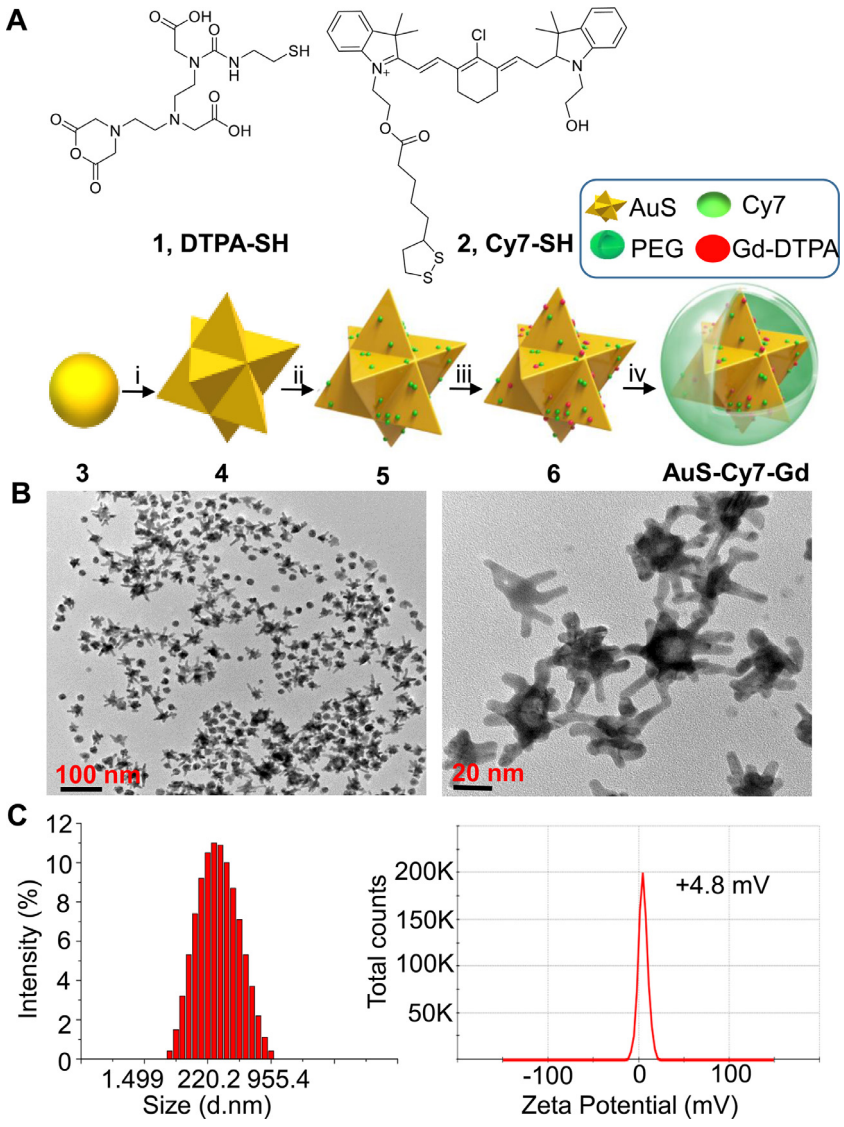

Fig. 2. Synthesis and characterization of the multimodal MR/SERRS probe AuS-Cy7-Gd. (a) Synthetic procedure of the target nanoprobe. (i) ascorbic acid, silver nitrate; (ii) Cy7-SH; (iii) DTPA-SH, $GdCl_3 \cdot 6H_2O$; (iv) mPEG-SH. (b) TEM images of AuS-Cy7-Gd. (c) Hydrodynamic particle size and zeta potential of AuS-Cy7-Gd.

2-aminoethanethiol [8]. AuSs were synthesized according to a so-called seed-meditated method reported previously [11]. Cy7-SH, a heptamethine cyanine dye-based Raman reporter that we previously reported [9], was subsequently attached to compound 4 via a Au-S bond to obtain compound 5, which was further reacted with DTPA-SH and $GdCl_3 \cdot 6H_2O$ to yield compound 6 via another Au-S bond. mPEG-SH was then attached to give 7, which finally yielded AuS-Cy7-Gd. TEM images showed that the nanoprobes were monodisperse with a star-shaped structure (Fig. 2b). The diameters of the nanoparticles were between 50 and 70 nm, with an average diameter of 60 nm, and each nanoparticle contained 10 prolate tips on average. The hydrodynamic diameter and zeta potential of the nanoparticles in aqueous solution were determined to be 220 nm and +4.8 mV respectively, (Fig. 2c). AuS-Cy7-Gd exhibited an absorption maximum centred at ~850 nm within the near-infrared (NIR) wavelength range (Figure S1). Ex vivo T1WI MR phantom images showed increased SI enhancement with increasing AuS-Cy7-Gd concentration, and the R_1 value was linearly associated with the concentration of AuS-Cy7 in aqueous solutions ($R^2 = 0.9050$) (Figure S2). As Figure S3 displays, AuS-Cy7-Gd maintained good monodispersity after one week, indicating the desirable stability of the nanoprobe. The XPS spectrum of AuNP and AuNP-Gd were shown in (Figure S4). For the AuNP (Fig S4a), XPS peaks for Au 4f7/2 and 4f5/2 were observed. For the AuNP-Gd (Fig S4b), additional peaks belong to Gd 4d were observed, verifying the success of Gd chelators conjugation to the AuNP. In vitro CCK-8 assay revealed no detectable cytotoxicity of AuS-Cy7-Gd to either tumour cells or normal cells even at highest concentration of 150 pM. (Figure S5). Similarly, H&E staining showed no obvious damage to the main organs of the rabbits after intravenous administration of AuS-Cy7-Gd. (Figure S6).

3.2. Tissue depth dependent Raman signal intensity and ex vivo cell phantoms

Evaluation of the largest depth for detecting a signal provided a good estimate of the imaging capabilities in deep tissues. Masseter muscle phantoms were then created. The bar chart was representative of the actual Raman intensity values used to produce the scaled graph (Figure S7). Data showed Raman signal intensity decreased 10.0%, 30.8% and 54.9% when tissue depth reached 0.3, 0.5 and 0.7 mm, respectively. However, the signal intensity dramatically decreased when the tissue depth is over 1 mm. Therefore, it was deemed that marginal tumour infiltration and micro

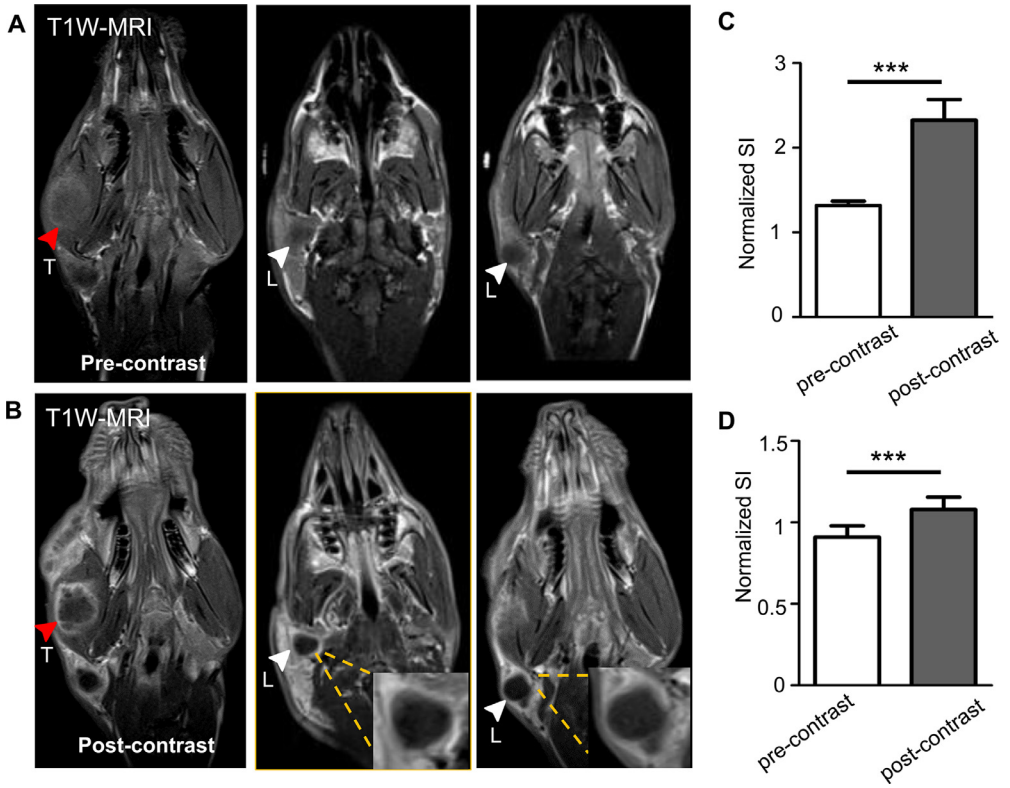

Fig. 3. AuS-Cy7-Gd preoperatively defined head and neck tumour margins and metastatic lymph nodes in rabbit models. T1-weighted MRI (T1W-MRI) of the head and neck region of the rabbit models before (a) and at 20 min after (b) the intravenous administration of AuS-Cy7-Gd. The tumour embedded in the right masseter muscle is denoted with a red arrowhead. Meanwhile, a metastatic lymph node in the right neck is indicated by a white arrowhead. ("T" stands for tumour; "L" stands for lymph node). Normalized T1W MR SI in the tumour (c) ($n = 15$) and metastatic lymph node (d) ($n = 12$) at 20 min post-injection of AuS-Cy7-Gd ($P < 0.001$). Statistical significance was calculated via a paired two-sample *t*-test. Note: *** indicates $p < 0.001$.

metastasis in resection bed within the depth of 1 mm would be possibly detected with application of SERRS guided surgical approach. For ex vivo cell phantom, greater signal intensities were observed with increasing numbers of AuS-Cy7-Gd treated VX-2 tumor cells (Figure S8). A linear relationship was observed between 1/T1 and cell numbers in the agarose gel phantoms ($r = 0.9779$, $P < 0.001$). Furthermore, ICP-MS revealed strong uptake of AuS-Cy7-Gd (20.7 pg Gd/per cell) by the VX-2 tumour cell.

3.3. Preoperative MR delineation of tumours and metastatic lymph nodes

To determine the ability of AuS-Cy7-Gd to preoperatively localize neck orthotopic tumour xenografts and metastatic lymph nodes, T1WI MR scans were performed pre- and 20-min post-intravenous administration of the nanoprobes (0.05 mmol [Gd^{3+}] per kg). As shown in Fig. 3a, a solid tumour with heterogeneous hypo-intensities was located in the right jugomaxillary muscle of a rabbit. Prior to administration of AuS-Cy7-Gd, the tumour margins in the T1WI MR images were blurred and could not be well defined. In addition to the primary tumour, an enlarged homolateral lymph node with heterogeneous hypo-intensities was visualized on the right side of the neck. Compared to the pre-contrast images, the contrast-enhanced T1WI images exhibited an obvious enhancement (approximately 80% increase in normalized SI) in the tumour marginal areas, delineating both the primary tumour and infiltrative margins of the tumour more clearly (Fig. 3b and c). For homolateral enlarged lymph nodes, only mild enhancement (an approximately 20% increase of normalized SI) in the marginal areas was observed in the lymph node, which is not sufficient to make a definite metastasis decision (Fig. 3b and d).

3.4. SERRS-guided precise tumour resection in intact living rabbits bearing VX2 tumours

The rabbit models bearing VX2 tumours were successfully established according to the methods mentioned above (Figure S9). Fig. 4 illustrates the step-by-step SERRS-guided surgical resection procedure. The corresponding SERRS spectrum (panel B) of the illuminated area was incorporated into the SERRS-guided surgical resection process (panel A). First, the primary tumour was subjected to resection with 90-degree laser beam illumination. Characteristic double peaks at 509 cm^{-1} and 541 cm^{-1}, were observed in tumour areas, representing the presence of AuS-Cy7-Gd in the tumour (Fig. 4). After the majority of the tumour was resected, the laser probe was adjusted to variable directions and angles to detect possible microscopic and satellite metastases around the infiltrative tumour margins. To ensure complete removal of the tumour, the tumour resection bed, especially the bottom and lateral parts, was detected until the SERRS signal was fully below the threshold (panel B, row four). Resected tumour tissues were subjected to H&E and immunohistochemical staining for further analysis. In accordance with the SERRS spectrum (panel B), representative H&E staining and Ki67 staining images verified that a clear pathological resection margin was finally acquired with the SERRS-guided surgical resection approach.

3.5. Accuracy of tumour margin assessment via the intra-operative SERRS-guided resection approach

H&E staining, TEM studies and in vitro confocal Raman imaging studies were performed to determine the accuracy of tumour margin assessment obtained via the SERRS-guided surgical

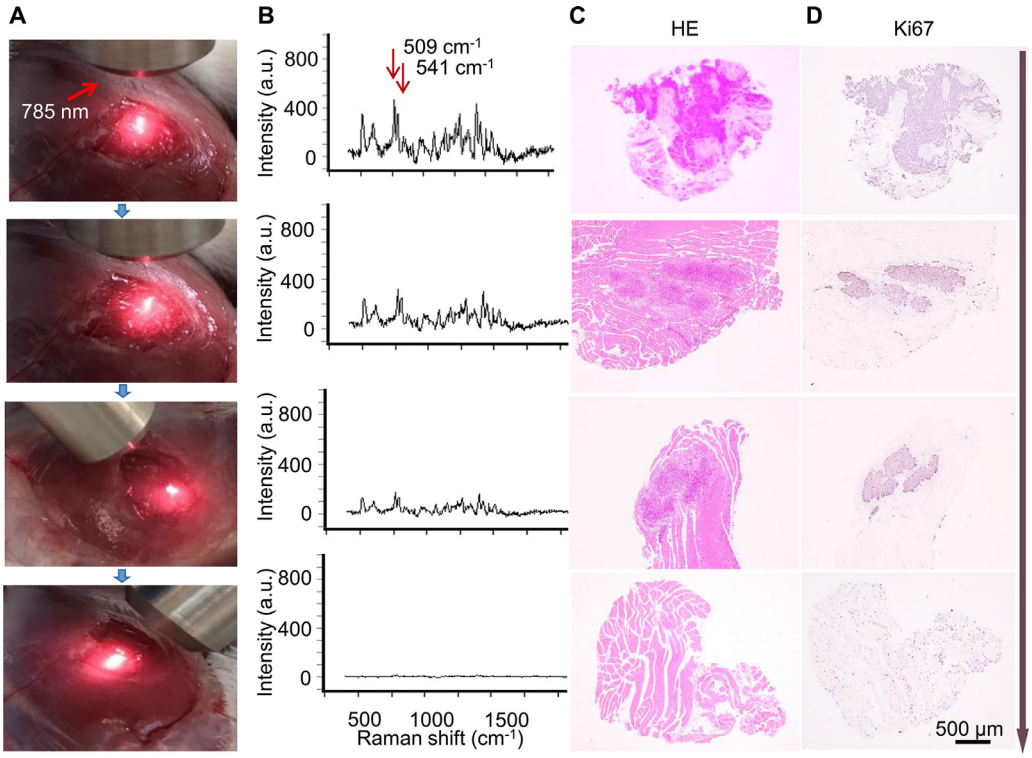

Fig. 4. AuS-Cy7-Gd intra-operatively guided head and neck tumour resection with the assistance of a hand-held Raman detector. (a) White-light images of the surgical procedure of Raman signal-guided tumour resection. The suspicious tissues were excited by a laser light with a wavelength of 785 nm. The surgery did not end until the characteristic signals of AuS-Cy7-Gd could not be detected in the resection bed. (b) Corresponding SERS spectra collected at different surgical stages. H&E (c) and Ki67 (d) staining images of the excised tissues with the sequence indicated in panel B. Scale bar: 500 μm.

resection approach. As shown in Fig. 5a and b, the tumour margins outlined in H&E staining images were fully identical to those in the confocal Raman mapping images, verifying the accuracy of the SERRS-guided resection approach in intra-operative margin assessment. The TEM images verified these results by showing the accumulation of abundant nanoprobes in the tumour tissues, whereas there were no detectable nanoprobes in the surrounding normal tissues (Fig. 5c and d). To further ensure whether the SERRS-guided resection approach could assess clear pathological margins, SERRS spectra and corresponding H&E staining images of the resection bed were acquired in the SERRS-guided resection and white-light-guided resection groups. Notably, the parts of the resection beds in the white-light-guided resection group exhibiting characteristic double peaks similar to the SERRS spectra of the primary tumour were pathologically confirmed to be satellite foci (Fig. 5f). In contrast, the SERRS-guided resection group showed no positive SERRS signals (SIs below threshold) in the resection beds and was pathologically confirmed to have clear resection margins (Fig. 5e). The data observed strongly indicated the superiority of the SERRS-guided resection approach compared to white-light-guided resection in intra-operatively assessing tumour margins and in detecting satellite metastases or infiltrative foci in tumour-surrounding areas, thereby offering a promising avenue for precise intra-operative tumour mapping.

3.6. Improved overall survival and prognosis with the SERRS-guided resection approach

To evaluate the influence of the white-light-guided resection and SERRS-guided surgical resection approaches on tumour prognosis, the survival time of the rabbits in the three groups was monitored until they died or the observation period ended. Then, tumour resection beds from rabbits treated with different resection approaches (white-light- or SERRS-guided resection) were sectioned and re-stained with H&E and Ki67 to determine tumour recurrence and tumour proliferation. Overall, tumour recurrence in the surgical resection bed was significantly lower in the SERRS-guided group than in the white-light guided group, as confirmed by the final histological analysis (10% vs 70%, $P<0.05$) (Fig. 5h). Moreover, a prolonged survival time was predominantly observed in the SERRS-guided group compared with in the control group (29 days) or the white-light-guided group (42 days), with a median survival time of 78 days ($P < 0.001$) (Fig. 5i), demonstrating that the SERRS-guided surgical resection approach enabled a great improvement in terms of tumour prognosis and survival.

3.7. SERRS-guided detection of cervical lymph nodes metastasis

To demonstrate the potential application of a Raman hand-held detector in the intra-operative detection of cervical lymph node metastasis, we performed the same SERRS-guided scanning of bilateral cervical neighbouring lymph nodes in orthotopic head and neck VX2 tumour xenografts using a 785-nm excitation laser Raman hand-held detector (Fig. 6a). As indicated in Fig. 6b, unique SERRS spectra of the nanoprobes were observed in lymph nodes that were histologically confirmed as non-metastatic lymph nodes, whereas decreased SERRS signals were observed in lymph nodes ultimately confirmed to be metastatic. Nodal metastases led to decreased accumulation of the lymphotropic SERRS nanoprobes and resulted in significantly lower SERRS SIs than those in the non-metastatic lymph nodes, which is consistent with the H&E staining results (Fig. 6c and d, $P < 0.001$).

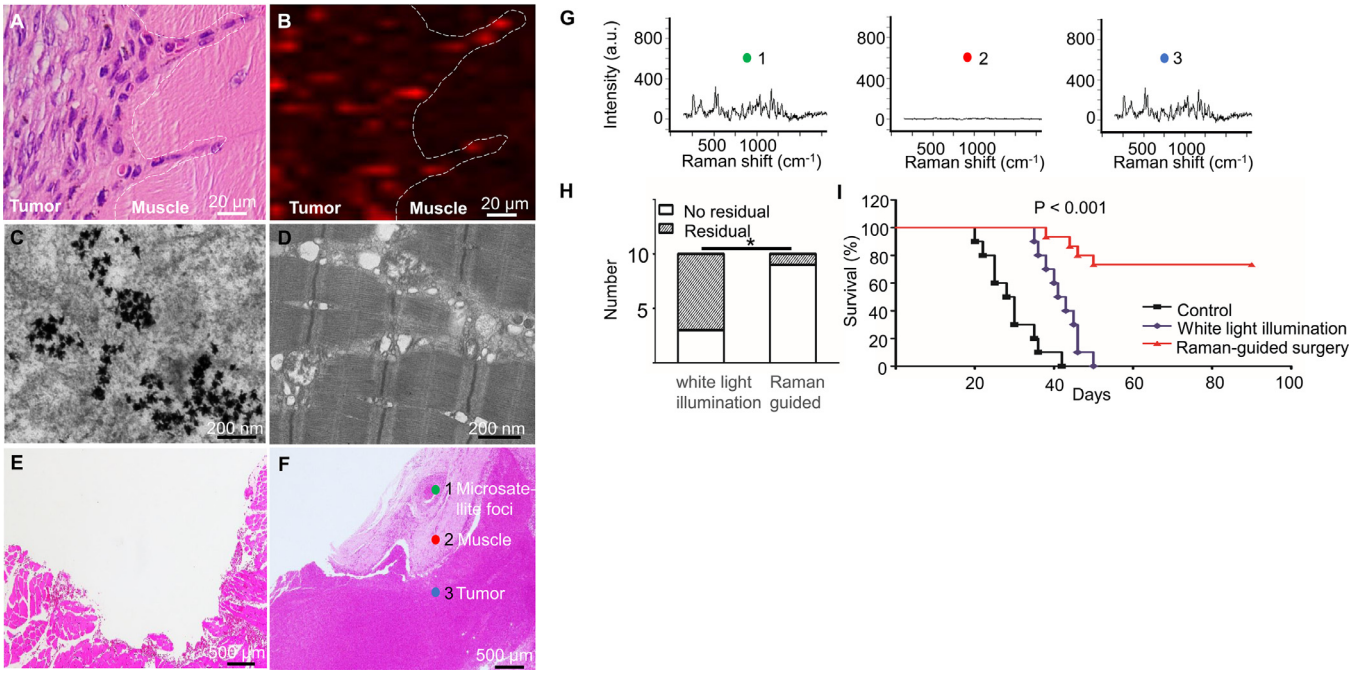

Fig. 5. AuS-Cy7-Gd accurately discriminates the boundary of head and neck tumour xenografts. H&E staining images (a) and Raman microscopy images (b) of tumour marginal tissues indicated that AuS-Cy7-Gd accurately demarcated tumour margins. TEM images of the tumour (c) and surrounding normal muscle tissue (d) at 24 h post-injection of AuS-Cy7-Gd. H&E staining of the tumour resection bed after AuS-Cy7-Gd-guided surgery (e) and white-light-guided surgery (f). (g) Corresponding SERRS spectrum collected at the green dot (1, microsatellite foci), red dot (2, normal muscle tissue) and blue dot (3, major focus) indicated in Figure 5F in the resection bed after the white-light guided surgery. (h) Kaplan–Meier curve estimates of survival of rabbit models after white-light- or Raman-guided surgery. Data are presented as the mean ± SD.

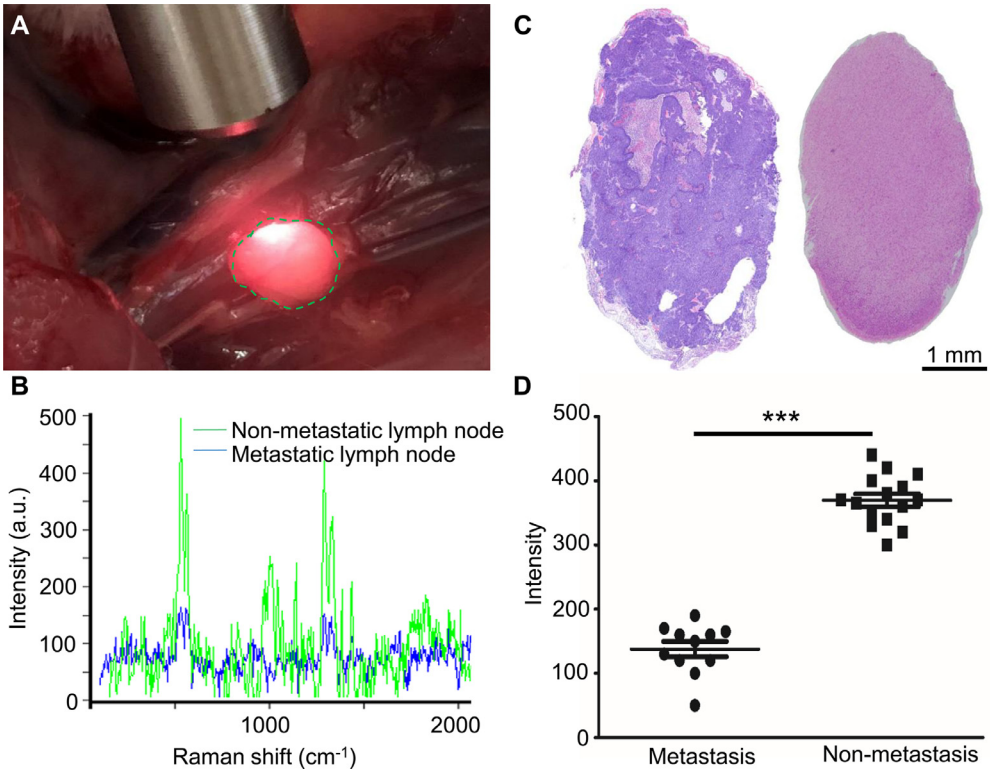

Fig. 6. AuS-Cy7-Gd intra-operatively visualized metastatic lymph nodes with hypo-intensive Raman signals. (a) Intra-operative detection of a metastatic lymph node by a hand-held Raman scanner. (b) Intra-operative Raman spectra of a metastatic lymph node (blue colour) in the tumour surgical bed and a non-metastatic lymph node (green colour) on the contralateral side. (c) H&E staining images of excised metastatic (l) and non-metastatic (r) lymph nodes. (d) SERRS intensities of the metastatic lymph nodes and non-metastatic lymph nodes ($P < 0.001$). Statistical significance was calculated via Student's *t*-test. Note: *** indicates $p < 0.001$.

4. Discussion

The completeness of tumour surgical resection is critical to HNSCC since it profoundly influences adjuvant treatment decisions and patient prognosis. Although preoperative MRI is valuable for identifying the localization and characteristics of primary neoplasms in the head and neck, many hurdles are still encountered, such as infiltrative tumour margins or invasion of adjacent neurological structures, making it difficult for surgeons to completely remove the tumour intra-operatively. Therefore, a more accurate or more optimized imaging-guided resection approach for HNSCC surgical management is clinically needed; in particular, an approach that integrates intra-operative imaging-guided resection and preoperative MRI with single-contrast-medium administration would be valuable.

In this work, to facilitate such a multi-modal strategy for HNSCC management, we presented a novel MR/SERRS nanoprobe, AuS-Cy7-Gd, that can be imaged using both MRI and Raman spectroscopy. Notably, AuSs were applied as the substrate of the SERRS probes in this study. The tip-enhanced plasmonics of star-shaped AuSs can strongly amplify their Raman signal, which is more than 100 times stronger than that of AuSs with a similar diameter and identical molecular reporter. Moreover, the plasmon absorption of AuSs in the NIR wavelength window (700–800 nm) resulted in great enhancement in the Raman SIs by maximizing the plasmon resonance with the incident laser (785 nm). In addition, Cy7-SH was chosen as the molecular reporter since its absorption maximum (790 nm) is approximately equal to the wavelength of the incident laser integrated into the hand-held Raman detectors. The resonances among the AuS, reporter molecule and incident laser further enhanced the Raman SIs and therefore provided ultra-high sensitivity for intra-operative Raman-guided surgical resection applications [6].

It is well understood that nanoparticles of a certain size and charge can specifically accumulate in cancer tissues but not in normal tissues. In our study, after a single ear-vein injection of AuS-Cy7-Gd into orthotopic VX2 tumour models, the nanoprobes predominantly accumulated in tumour tissues but not in healthy tissues via the enhanced permeability and retention (EPR) effect [14]. The TEM study verified that the nanoprobe accumulated abundantly in tumour tissues but was not detectable in normal tissues, making the nanoprobe tumour specific. Because Gd^{3+} was functionalized on the nanoprobe, it could serve as an MRI contrast agent for preoperative imaging. Representative MR images demonstrated heterogeneous hypo-intensities and blurred tumour boundaries of primary HNSCC tumours in T1-weighted non-contrast MR images. Compared to primary solid tumours, suspected cervical metastatic lymph nodes presented uneven internal SIs in T1WI non-contrast images. After intravenous administration of AuNS-Cy7-Gd, the SIs from the primary tumours were significantly enhanced (more than twice the normalized SI), and the infiltrative margins of HNSCC were more clearly delineated. Moreover, the unclear margins of homolateral cervical lymph nodes in the non-enhanced T1 images were better delineated in the T1-enhanced MR images, indicating the excellent ability of the nanoprobe for macroscopic delineation using MRI.

To determine whether SERRS-guided surgical resection is feasible in HNSCC, we established a step-by-step SERRS-guided resection procedure in rabbit models bearing VX2 tumours with the assistance of a hand-held Raman detector. Obviously, the fingerprint-like characteristic double peaks at 509 cm^{-1} and 541 cm^{-1} were clearly observed in solid tumours but not in the surrounding normal tissue [7,15]. Furthermore, our data presented a corresponding decrease in SERRS signal intensities with the tumour removal process. After the majority of the tumour is removed, management of the resection bed is important for surgeons. Instead of extended resections, we analysed the resection bed by adjusting the flexible laser probe to variable angles to search for obvious SERRS signals until all the signals were lower than the threshold (SI of normal muscles). Both the H&E and Ki67 staining results confirmed the clear pathological resection margin obtained via the SERRS-guided resection approach. In contrast, after white-light-guide resection, we were still able to detect tiny residual lesions around the primary tumour in the white-light guided resection group by SERRS signals, and these lesions were finally confirmed as millimetre-scale satellite metastatic foci. As reported, residual tumours as small as 100 μm can be detected by SERRS imaging, thereby minimizing the high risk of tumour tissue left behind in the resection bed [6,16]. Moreover, nearly completely overlapping tumour boundaries were observed with in vitro Raman mapping and HE staining, assuring the preciseness of the SERRS-guided resection approach. To further understand the effect of the SERRS-guided resection approach on the prognosis of HNSCC, tumour recurrence in the resection bed and median survival time were compared among the white-light-guided resection, SERRS-guided resection and control groups. A much lower tumour recurrence rate was observed in the SERRS-guided resection group than in the control group (10% vs 70%, $P < 0.05$), verifying the superior removal completeness enabled by the SERRS guidance. Moreover, the results clearly showed that the application of the SERRS-guided surgical resection approach significantly improved survival, with a prolonged mean survival time of 78 days, ensuring the value of the multi-modal nanoprobe in improving HNSCC surgical prognosis.

Based on the results in previous studies, cervical lymph node metastasis actually occurs in approximately 50% of HNSCC patients at the onset. Although preoperative imaging assists surgical planning, enlarged lymph nodes are poorly distinguished from reactive inflammatory lymph nodes or normal lymph nodes by either CT or MRI, resulting in incomplete detection of metastatic lymph nodes. The naturally lymphotropic SERRS nanoprobes accumulated in the reticuloendothelial system (RES) [17,18]. Nodal metastases altered the internal architecture of lymph nodes, allowing us to detect abnormal lymph node metastasis by decreasing SERRS signals. Similarly, intravenously administered superparamagnetic iron oxide nanoparticles (SPIONs), which are normally extravasated from the vasculature into the interstitial space, went through the lymphatic system and were finally internalized by macrophages, leading to homogeneous low SIs in T2-weighted images of normally functioning lymph nodes. Therefore, altered signal intensities on T2-weighted images allowed the detection of partial or complete metastasis in lymph nodes by MRI [19–23]. However, MRI could not provide an intra-operative identification for lymph node status. Our data showed that via a hand-held detector, SERRS SIs generated by AuS-Cy7-Gd can well discriminate between cervical metastatic lymph nodes and non-metastatic lymph nodes, which is corroborated with the results of histological analysis, offering us a real-time intra-operative modality for surgical management. Spaliviero et al. [18] also demonstrated the decreased accumulation of a SERRS probe in iliac lymph nodes infiltrated by PC-3 prostate cancer cells and a significant reduction in SEERS SIs compared to those in healthy lymph nodes. Notably, the lymph nodes observed in our VX2 rabbit models ranged in size from 2.1–3 mm along the short axis, which was approximately 5-fold smaller than those in humans, showing the superiority of SERRS in the fast intra-operative detection of lymph node metastasis. In another clinical trial, a Raman spectroscopic probe was used to map axillary lymph nodes in patients with breast cancer, and using a multi-point probe model (selecting multiple points on the lymph nodes to probe) was shown to greatly enhance the differentiation accuracy, demonstrating up to 91% agreement with histological assessment and thus showing the high prospects of SERRS nanoprobes for potential clinical translation [24].

5. Conclusions

Overall, the MR/SERRS nanoprobe with multi-modal potential developed in this study enabled preoperative MRI and intraoperative image-guided resection of head and neck tumour xenografts by virtue of the SERRS effect. The ability of the nanoprobe to precisely define infiltrative tumour margins and metastatic lymph nodes would markedly reduce the need for unnecessary resection in the head and neck area and profoundly improve the surgical prognosis of head and neck carcinoma.

Funding

The study is supported by the National Natural Science Foundation of China (No. 91859202, 81771901 to XF.T; 81771963 to YW.W) and the Clinical Research Program of Shanghai Ninth People's Hospital, Shanghai Jiao Tong University, School of Medicine (No. JYLJ033).

Role of the Funding Source

The study sponsors had no involvement in the study design; collection, analysis and interpretation of data; the writing of the manuscript; the decision to submit the manuscript for publication.

Declaration of Competing Interest

The authors declare no conflicts of interest.

CRediT authorship contribution statement

Pengpeng Sun: Formal analysis, Project administration. **Yunfei Zhang:** Formal analysis, Project administration. **Kaicheng Li:** Formal analysis, Project administration. **Cong Wang:** Project administration, Validation. **Feng Zeng:** Project administration, Validation. **Jinyu Zhu:** Project administration, Validation. **Yingwei Wu:** Project administration, Writing - original draft. **Xiaofeng Tao:** Supervision, Writing - review & editing.

Author Contributions

XFT designed the project, interpreted results and review the manuscript. YWW, designed experiments, analysed the data, and wrote the manuscript. PS, YFZ and KCL performed experiments and analysed the data. CW, JYZ and FZ conducted synthesis and characterization of the nanoprobe and assisted with experimental work. All authors discussed the results and commented on the manuscript.

Supplementary materials

Supplementary material associated with this article can be found, in the online version, at doi:10.1016/j.ebiom.2019.10.055.

References

[1] Leemans CR, Snijders PJF, Brakenhoff RH. The molecular landscape of head and neck cancer. Nat Rev Cancer 2018;18:269–82.
[2] Ragin CCR, Modugno F, Gollin SM. The epidemiology and risk factors of head and neck cancer: a focus on human papillomavirus. J Dent Res 2007;86:104–14.
[3] Cancer Genome Atlas Network Comprehensive genomic characterization of head and neck squamous cell carcinomas. Nature 2015;517:576–82.
[4] Woolgar JA, Triantafyllou A. A histopathological appraisal of surgical margins in oral and oropharyngeal cancer resection specimens. Oral Oncol 2005;41:1034–43.
[5] Curtin HD, Ishwaran H, Mancuso AA, Dalley RW, Caudry DJ, McNeil BJ. Comparison of CT and MR imaging in staging of neck metastases. Radiology 1998;207:123–30.
[6] Harmsen S, Huang R, Wall MA, et al. Surface-enhanced resonance Raman scattering nanostars for high-precision cancer imaging. Sci Transl Med 2015;7:271r–277r.
[7] Kircher MF, de la Zerda A, Jokerst JV, et al. A brain tumor molecular imaging strategy using a new triple-modality MRI-photoacoustic-Raman nanoparticle. Nat Med 2012;18:829–34.
[8] Yue Q, Gao X, Yu Y, et al. An EGFRvIII targeted dual-modal gold nanoprobe for imaging-guided brain tumor surgery. Nanoscale 2017;9:7930–40.
[9] Zhang Y, Liu H, Tang J, et al. Noninvasively imaging subcutaneous tumor xenograft by a handheld Raman detector, with the assistance of an optical clearing agent. ACS Appl Mater Interfaces 2017;9:17769–76.
[10] Karabeber H, Huang R, Iacono P, et al. Guiding brain tumor resection using surface-enhanced raman scattering nanoparticles and a hand-held Raman scanner. ACS Nano 2014;8:9755–66.
[11] Yuan H, Khoury CG, Hwang H, Wilson CM, Grant GA, Vo-Dinh T. Gold nanostars: surfactant-free synthesis, 3D modelling, and two-photon photoluminescence imaging. Nanotechnology 2012;23:75102.
[12] Zheng L, Sun P, Zheng S, Han Y, Zhang G. Functional dynamic contrast-enhanced magnetic resonance imaging in an animal model of brain metastases: a pilot study. PLoS ONE 2014;9:e109308.
[13] Zheng L, Li Y, Geng F, et al. Using semi-quantitative dynamic contrast-enhanced magnetic resonance imaging parameters to evaluate tumor hypoxia: a preclinical feasibility study in a maxillofacial Vx2 rabbit model. Am J Transl Res 2015;7:535–47.
[14] Fang J, Nakamura H, Maeda H. The EPR effect: unique features of tumor blood vessels for drug delivery, factors involved, and limitations and augmentation of the effect. Adv Drug Deliv Rev 2011;63:136–51.
[15] Zavaleta C, de la Zerda A, Liu Z, et al. Noninvasive Raman spectroscopy in living mice for evaluation of tumor targeting with carbon nanotubes. Nano Lett 2008;8:2800–5.
[16] Oseledchyk A, Andreou C, Wall MA, Kircher MF. Folate-targeted surface-enhanced resonance Raman scattering nanoprobe ratiometry for detection of microscopic ovarian cancer. ACS Nano 2017;11:1488–97.
[17] Andreou C, Pal S, Rotter L, Yang J, Kircher MF. Molecular imaging in nanotechnology and theranostics. Mol Imaging Biol 2017;19:363–72.
[18] Spaliviero M, Harmsen S, Huang R, et al. Detection of lymph node metastases with SERRS nanoparticles. Mol Imaging Biol 2016;18:677–85.
[19] Wunderbaldinger P, Josephson L, Bremer C, Moore A, Weissleder R. Detection of lymph node metastases by contrast-enhanced mri in an experimental model. Magn Reson Med 2002;47:292–7.
[20] Zhang F, Zhu L, Huang X, Niu G, Chen X. Differentiation of reactive and tumor metastatic lymph nodes with diffusion-weighted and SPIO-enhanced MRI. Mol Imaging Biol 2013;15:40–7.
[21] Motomura K, Izumi T, Tateishi S, et al. Correlation between the area of high--signal intensity on spio-enhanced MR imaging and the pathologic size of sentinel node metastases in breast cancer patients with positive sentinel nodes. BMC Med Imaging 2013;13:32.
[22] Motomura K, Ishitobi M, Komoike Y, et al. Spio-enhanced magnetic resonance imaging for the detection of metastases in sentinel nodes localized by computed tomography lymphography in patients with breast cancer. Ann Surg Oncol 2011;18:3422–9.
[23] Taupitz M, Wagner S, Hamm B, Dienemann D, Lawaczeck R, Wolf KJ. Mr lymphography using iron oxide particles: detection of lymph node metastases in the VX2 rabbit tumor model. Acta Radiol 1993;34:10–15.
[24] Horsnell JD, Smith JA, Sattlecker M, et al. Raman spectroscopy–a potential new method for the intra-operative assessment of axillary lymph nodes. Surgeon 2012;10:123–7.